Plasma Phys. Control. Fusion **48** (2006) 1165–1180 doi:10.1088/0741-3335/48/8/009

Spectroscopic measurement of atomic and molecular deuterium fluxes in the DIII-D plasma edge

E M Hollmann[1], S Brezinsek[2], N H Brooks[3], M Groth[4], A G McLean[5], A Yu Pigarov[1] and D L Rudakov[1]

[1]University of California, San Diego, California, USA
[2]Institut für Plasmaphysik, Forschungszentrum Jülich, Jülich, Germany
[3]General Atomics, San Diego, California, USA
[4]Lawrence Livermore National Laboratory, Livermore, California, USA
[5]University of Toronto (UTIAS), Toronto, Canada

Received 6 April 2006,, in final form 9 June 2006
Published 14 July 2006
Online at stacks.iop.org/PPCF/48/1165

Abstract
Molecular deuterium fluxes into the edge of deuterium-fuelled L-mode discharges are measured using passive visible spectroscopy of D_2 emission lines. Comparison with the atomic deuterium influx measured using D_α emission suggests that a significant fraction of the plasma edge fuelling from the walls is in the form of D_2. Molecular deuterium flux is observed in both the divertor and main chamber regions but is roughly a factor 100 smaller near the inner main chamber wall and roughly a factor 1000 smaller near the outer main chamber wall, when compared with the divertor region. Very high levels of molecular D_2 excitation are measured, with ground state D_2 rotational population temperatures T_{rot} up to 10 000 K and vibrational population temperatures T_{vib} up to 30 000 K. Comparisons between rotational population temperatures and the local electron density suggest that T_{rot} can be used as a reasonably good indicator of electron density in the D_2 line emission region. In recombining, detached divertor operation, estimates of the enhanced volume recombination rate due to the presence of vibrationally-excited D_2 suggest that the effect of molecular-assisted volume recombination could be comparable in magnitude to that of normal D^+ volume recombination (EIR).

1. Introduction

In tokamak discharges, molecular hydrogen H_2 (or isotopes thereof) is the main fuelling species, dominantly resulting from plasma recycling on the vessel walls and from gas puffing. The spatial distribution of molecular hydrogen (and the resulting distribution of atomic hydrogen) in the plasma edge region plays a central role in plasma performance, affecting pedestal shape and core density control [1]. Despite general consensus on the importance of the H_2 and H spatial distributions on plasma performance, uncertainties remain in the details of what determines these spatial distributions and how these in turn affect the core plasma. For example, wall pumping of hydrogen [2], the relative importance of main chamber plasma recycling versus neutral 'leakage' into the main chamber [3–5], and ultimately the effect on pedestal shape [6] are all active areas of research. These studies are important for the design of future fusion reactors because the pedestal shape affects the volume-integrated plasma pressure (thus affecting fusion gain) and also affects the frequency and intensity of edge localized modes (ELMs), which affect wall erosion and lifetime.

In addition to its role in edge fuelling, molecular hydrogen is important for plasma edge atomic physics. An example of this is molecular-assisted recombination (MAR), the enhancement of plasma volume recombination believed to occur in the presence of vibrationally-excited hydrogen molecules via conversion of H^+ ions into molecular ions such as H_2^+ and H_3^+ [7]. Some uncertainty remains as to the importance of MAR in tokamak divertors: experiments in ASDEX-U have suggested only a small ($\approx$ 10%) increase in divertor volume recombination rate due to MAR [8], while experiments in JT-60U have suggested a more significant ($2\times$) increase [9].

Here, measurements of the D_2 molecule flux into the far edge/scrape-off layer (SOL) of the DIII-D tokamak [10] during deuterium-fuelled L-mode, lower-single-null diverted discharges are made using passive visible spectroscopy of the D_2 diagonal Fulcher band together with calculated emission rate coefficients and measured edge profiles of electron density and electron temperature. Deuteron influx from D_2 is found to be comparable to that from D, consistent with wall emission dominantly in the form of D_2, with D resulting mostly from D_2 breakup. In recombining (detached) divertor operation, the divertor D_2 flux and vibrational population temperature is used to estimate the magnitude of MAR, while the measured D_γ and D_ε brightnesses are used to estimate standard D^+ recombination (EIR). These estimates suggest that MAR could be comparable in magnitude to EIR in detached DIII-D divertors.

2. Experimental Setup

The main diagnostic used here is a 1.3 m Czerny–Turner type multi-chord visible spectrometer with views of both lower divertor legs (chords 1–7) and the main chamber (chords 8–11) [11]. The instrument has a spectral resolution $\Delta\lambda \approx 0.01$ nm and covers a wavelength range of about 10 nm for each grating position. An integration time of 100 ms is typically used. Other spectrometers used are a survey spectrometer with wavelength coverage of 300–800 nm in a single image and spectral resolution $\Delta\lambda \approx 2.6$ nm and a near-UV spectrometer with good sensitivity of around 340 nm, coverage of about 5 nm for each grating position and spectral resolution $\Delta\lambda \approx 0.1$ nm; both these latter spectrometers were set up with single-chord views of the outer divertor leg. Additionally, Thomson scattering [12] and plunging Langmuir probes [13] are used to measure the electron density n_e and electron temperature T_e in the plasma edge region. Images of D_2 emission from the lower divertor region are obtained with a tangentially-viewing CID camera [14, 15]. A schematic of the spectrometer view chords used, as well as typical magnetic flux surfaces, midplane probe location, Thomson scattering view locations, midplane neutral pressure gauge and divertor camera view are shown in figure 1. The tangential view chords see D_α and C_{III} emission via filterscopes (photomultiplier tubes viewing the plasma through visible bandpass filters). As a convenient variable to describe the location of each view chord, the poloidal angle θ of the approximate expected dominant emission volume is used, as shown by dark-shaded circles in figure 1. White circles in figure 1 indicate the approximate location of the expected secondary (weaker) emission volume for the same view chord. The assumption that D and D_2 line emission in the lower (divertor region) SOL is stronger than the upper main chamber SOL is justified by the visible camera

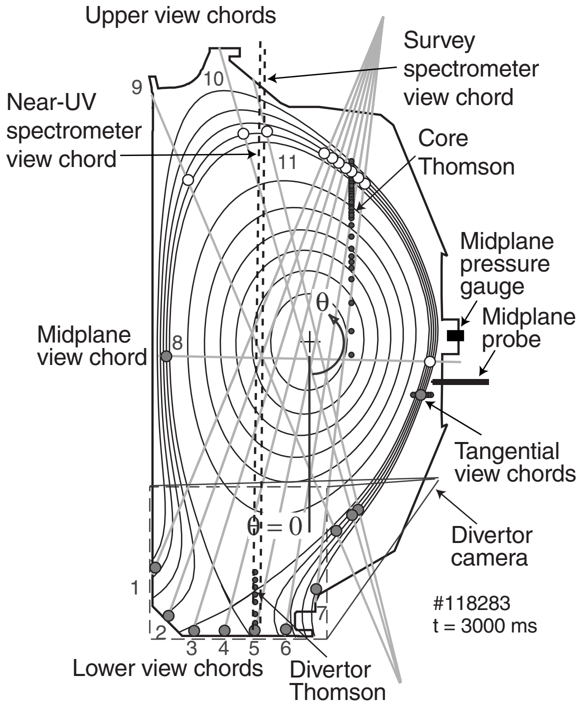

Figure 1. Schematic of visible spectrometer view chords, Thomson scattering view points, midplane probe location and divertor camera view. Shaded circles indicate approximate dominant emission region locations measured by visible spectrometer.

inversions of D_α emission during discharges similar to those studied here, which find that upper main chamber SOL D_α emission is significantly ($> 100\times$) weaker than that from the lower SOL/divertor region. The assumption that the midplane view chord measures D and D_2 line emission mostly from the centre post, as opposed to the outer midplane, is justified in section 4.

To achieve good divertor diagnostic measurements and stable edge conditions (e.g. no ELMs), L-mode, lower-single-null diverted discharges are used with $\approx$ 3s current flat-tops to allow for long integration times and sufficiently large signals with the spectrometer. Typical plasma parameters are toroidal magnetic field $B_\mathrm{T} = 2\,\mathrm{T}$, plasma current $I_\mathrm{p} = 1.1\,\mathrm{MA}$, line-averaged electron density $\bar{n}_\mathrm{e} = (2\text{–}5) \times 10^{19}\mathrm{m}^{-3}$ and central temperature $T_{\mathrm{e},0} = 1\text{–}2.5\,\mathrm{keV}$. Input power is typically $P_\mathrm{heat} = 1\text{–}3\,\mathrm{MW}$ from Ohmic heating combined, on some shots, with a single neutral beam.

3. Analysis of D_2 Spectral Data

The diagonal Fulcher-α band of D_2[(1s)3p–(1s)2s triplet Q-branch, $d^3\,\Pi_u^- \rightarrow a^3\Sigma_g^+$] covers the wavelength range $\lambda \approx$ 600–640nm. A composite spectrum of the Fulcher band obtained from six repeat shots (in which the spectrometer grating was advanced between shots) is shown in figure 2 with some of the strongest lines labelled, e.g. $Q6(1\text{–}1)$ refers to the $[(1\mathrm{s})3\mathrm{p}, \mathrm{v}' = 1, \mathrm{J}' = 6] \rightarrow [(1\mathrm{s})2\mathrm{s}, \mathrm{v}'' = 1, \mathrm{J}'' = 6]$ transition, where v and J are the vibrational and rotational quantum numbers with the prime (or double prime) denoting values

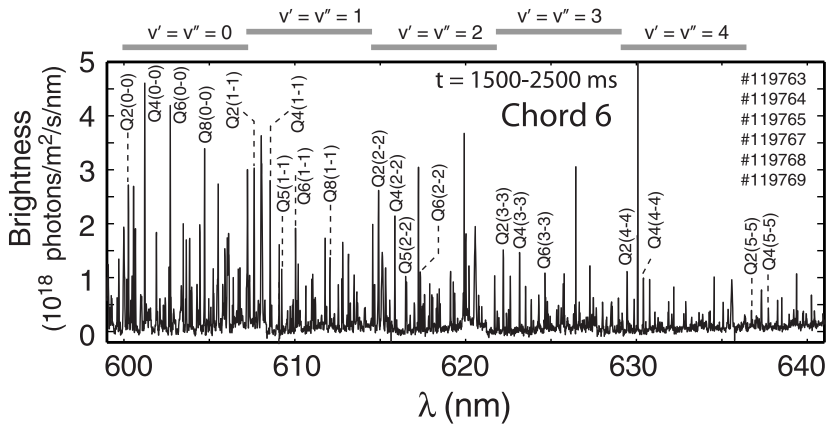

Figure 2. Survey of D_2 Fulcher band seen with visible spectrometer in attached divertor (composite of six spectral windows from series of six repeat shots).

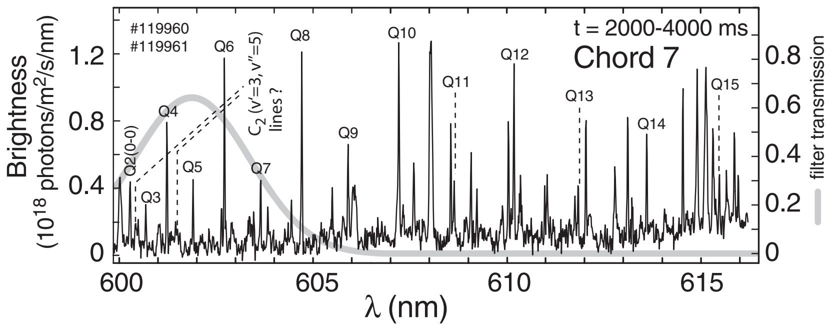

Figure 3. Spectrum of $v' = 0$ branch of D_2 Fulcher band seen in detached divertor (composite of two overlapping spectral windows from two repeat shots). Interference filter is used to obtain D_2 images with divertor camera.

in the electronic excited (1s)3p [or (1s)2s] states. A detailed spectrum of a single vibrational branch ($v' = v'' = 0$) is shown in figure 3. In this case, data was taken in a detached divertor discharge and two repeat shots were used to span 15 nm with the spectrometer.

Measured Fulcher band line brightnesses are converted into edge D_2 fluxes by summing over lines to estimate the total band brightness and then multiplying the total band brightness by a *D/XB* (dissociation events per Fulcher photon) conversion factor. Summing over line brightnesses is typically done by fitting to a different rotational temperature for each upper state vibrational level to describe the (rotationally summed) level densities in the ground electronic state [(1s)1s or $X^1\,\Sigma_g^+$] [16]. The ground electronic state vibrational level densities are mapped to the (1s)3p state using the vibrationally-resolved Franck–Condon matrix for electron-impact excitation [17]. Typically, these functional forms are found to describe the measured line brightnesses reasonably well. Sample fits are shown in figure 4(*a*) for the (1s)3p state rotational temperature for the first four (1s)3p state vibrational levels $v' = 0 - 3$ for the (attached divertor) data of figure 2. Lines up to $Q8$ or $Q9$ can usually be resolved reasonably well. Figure 4(*b*) shows a single rotational temperature fit to the (detached divertor) data of figure 3. In this case, lines up to $Q15$ could be resolved. Figure 4(*c*) shows a fit for the $(1s)1s$ state vibrational temperature for the first four vibrational levels ($v' = 0$ to $v' = 3$)

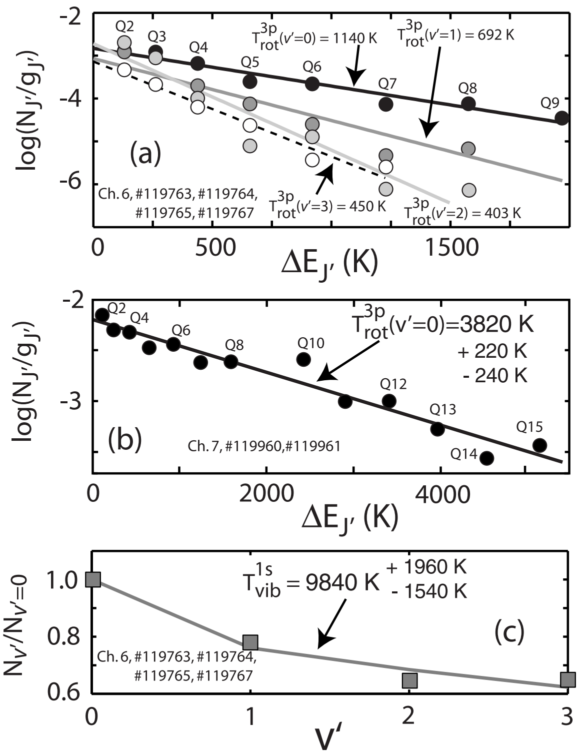

Figure 4. (*a*) Single rotational temperature fits to first four vibrational levels in attached divertor; (*b*) single rotational temperature fit to $v' = 0$ in detached divertor; (*c*) single-vibrational temperature fit to relative densities of first four vibrational levels for attached divertor. $N_{J'}$ ($N_{V'}$) are rotationally (vibrationally) resolved level densities in the electronic excited ls(3p) state, $g_{J'}$ are statistical weights and $\Delta E_{J'}$ the rotational energy relative to $J' = 0$. Lines correspond to fits and points correspond to measured data.

again using the data of figure 2. Rotationally off-diagonal (P and R) branches are not fit explicitly but are accounted for using a factor 2 correction [18]. The decreasing trend in T_{rot} with vibrational state v' seen in figure 4(*a*) is observed in most of the DIII-D data and is consistent with a variety of previous experiments [19–21]. It has been hypothesized that this trend is caused by a v dependence on rotational excitation/de-excitation rates, although this has not been confirmed and is not included in present simulations of rotational excitation of hydrogen molecules [22]. In some cases, a two rotational temperature (bi-Boltzmann) fit is found to match the (1s)$3p(v = 0)$ brightness data somewhat better, with the 'knee' in the distribution typically occurring around $Q7$ (a suggestion of this can be seen in the data of figures 4(*a*) and (*b*)); however, for the work done here, single rotational temperature fits over the levels $Q2 - Q9$ are used, since using a bi-Boltzmann fit was not found to change the total estimated Fulcher band brightness significantly. In general, Fulcher band brightness data for each shot is averaged over the entire current flat-top time to get the best possible fits to T^{1s}_{vib} and T^{3p}_{rot}.

As seen in figure 2, measurable line emission is readily observed up to the 6th(1s)$3p$ state vibrational level ($v' = 5$) of the Fulcher band. The measured emission for higher vibrational states is very weak, probably due to predissociation, and is not useful for fitting to the vibrational temperature. Often it is not practical to depend on repeat shots to measure

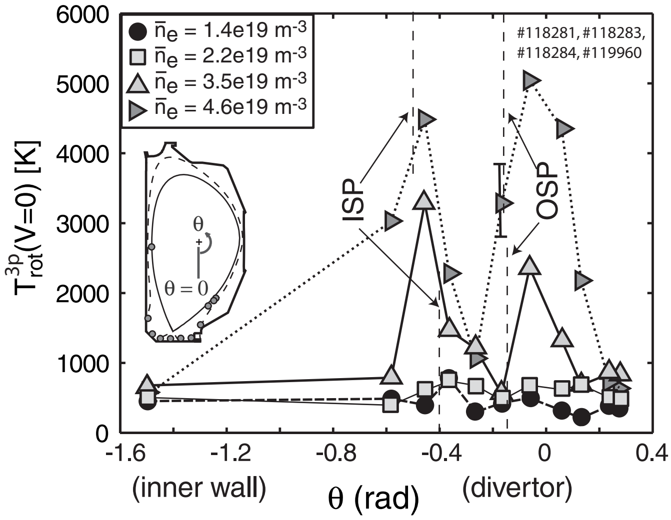

Figure 5. Upper electronic state D_2 rotational temperature $T^{3p}_{rot}(v' = 0)$ as a function of poloidal angle θ for four different (line-averaged) discharge densities. Upper locations of inner and outer strike points (ISP, OSP) correspond to highest density case.

the entire band, so only the first ($v' = 0$) branch is measured. In this case, the empirical linear scaling $T^{1s}_{vib} \approx 8T^{3p}_{rot}(v' = 0) - 1640$ K for T^{1s}_{vib} versus single rotational temperature fits $T^{3p}_{rot}(v' = 0)$ found in TEXTOR experiments for plasmas with $n_e \approx (0.1\text{–}1.5) \times 10^{19}$ m^{-3} and $T_e \approx 30\text{–}80$ eV is used to estimate the entire band brightness [21]. A scaling allowing for bi-Boltzmann fits to rotational temperature has not been performed yet and will need to be studied in future work. The TEXTOR scaling was checked for four L-mode discharges where enough repeat shots were obtained to gather data over the first four vibrational levels ($v' = 0$ to $v' = 3$). Single vibrational temperature fits to ($v' = 0$ to $v' = 3$) such as shown in figure 4(*c*) were used to estimate the entire band intensity ($v' = 0$ to $v' = 5$). Although the parameter range of the DIII-D data was different, with local electron densities $n_e \approx (0.2\text{–}12) \times 10^{19}$ m^{-3} and electron temperatures $T_e \approx 5\text{–}60$ eV, the TEXTOR scaling was found to estimate T^{1s}_{vib} (and the total band brightness) within $\approx 2\times$.

$T^{3p}_{rot}(v' = 0)$ is observed to increase with increasing line-averaged electron density $\bar{n}_e$ in the DIII-D experiments (as is T^{1s}_{vib} in the shots where sufficient data was obtained to independently determine T^{1s}_{vib}). Figure 5 shows the measured rotational population temperature $T^{3p}_{rot}(v' = 0)$ as a function of poloidal angle for four different line-averaged electron densities $\bar{n}_e$. It can be seen that $T^{3p}_{rot}(v' = 0)$ increases with increasing average electron density and is also larger in the dense divertor region than in the main chamber SOL. This is consistent with previous experiments [21,23] and simulations [22], which have indicated that the rotational temperature of the neutral molecules increases monotonically (roughly linearly) with increasing electron density but depends only weakly on the electron temperature. The other rotational temperatures $T^{3p}_{rot}(v' > 0)$ are also observed to increase with increasing electron density. The basic mechanism for this increase is thought to be that the heat source (collisions with plasma) increases with electron density, while the heat sink (the wall) does not depend on electron density. According to the simulations, this increase continues up to a very high (depending on the thickness of the D_2-plasma interaction region) electron density at which point $T^{3p}_{rot}(v' = 0)$ saturates (this saturation has not been observed yet experimentally). Characteristic error bars

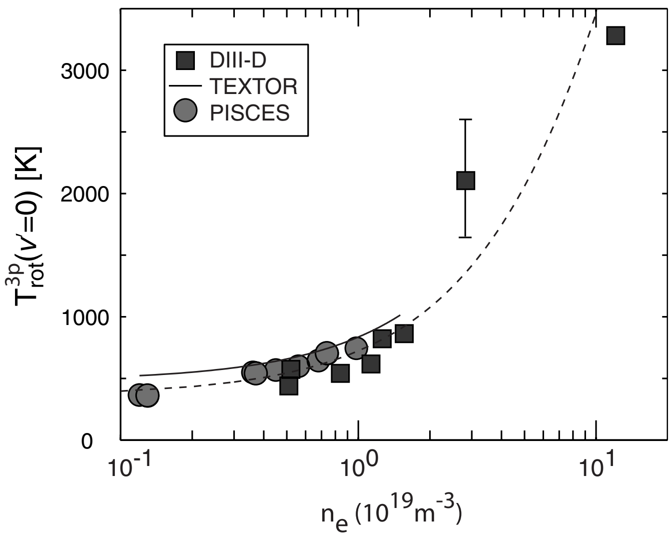

Figure 6. Upper electronic state D_2 rotational temperature $T_{rot}^{3p}(v' = 0)$ as a function of local electron density in emission region.

for $T_{rot}^{3p}(v' = 0)$ in figure 5 are estimated based on the accuracy of the linear (single rotational temperature) fit to the levels $Q2$-$Q9$. The estimated error is typically less than $\pm 20\%$.

The dependence of $T_{rot}^{3p}(v' = 0)$ of D_2 on the local electron density n_e was estimated by comparing $T_{rot}^{3p}(v' = 0)$ from view chord 5 (which views the outer divertor strike point in these discharges, as shown in figure 1) with n_e measured locally with Thomson scattering. For attached outer divertor legs ($T_e > 5$ eV at target plate), the D_2 emission is assumed to be localized to the divertor plate. For detached outer divertor legs, the D_2 emission is assumed to come from the first point on the Thomson profile where $T_e > 5$ eV, i.e where the divertor leg transitions from recombining to ionizing. D_2 emission from regions with $T_e < 5$ eV is expected to be small because the threshold energy for excitation of Fulcher band emission is ≈ 15 eV. The resulting $T_{rot}^{3p}(v' = 0)$ versus n_e DIII-D data is shown by squares in figure 6. For comparison, measurements using H_2 (note that the temperature $T_{rot}^{3p}(v' = 0)$ of H_2 is expected to be slightly larger than that for D_2) in the PISCES-A linear divertor simulator experiment [22] are shown (as circles) and the scaling found in TEXTOR D_2 discharges is shown by a solid line. The dashed curve is a fit to the data, which is used here to estimate n_e in the D_2 line emission region. The increase in $T_{rot}^{3p}(v' = 0)$ is roughly linear in n_e, although this is not immediately apparent in figure 6 because of the log axis.

The slight differences in the data from the different machines could be due to differences in wall temperature and differences in the hydrogen isotope used. The TEXTOR data was taken in front of a graphite test limiter at about 620 K, which is hotter than the graphite plasma-facing surfaces used in the DIII-D experiments ($\approx$ 400–500 K). Hotter emitting surfaces have been demonstrated to increase the resulting T_{rot} [24]. In the case of the PISCES data, the wall is cold stainless steel ($\approx$ 300 K), which should give lower T_{rot}. However, the measured isotope is H_2, rather than D_2, and experiments have suggested a roughly 10% larger T_{rot} for H_2 compared with D_2 in the same plasma conditions [21].

4. Measurements of deuteron flux into ionizing edge plasmas

The *D/XB* factor used to convert total Fulcher band brightnesses into *D* fluxes is obtained from an experimentally verified [16] collisional-radiative model [25]. The collisional-radiative model includes electronic levels 1, 2, 3 and ∞. Vibrational levels are included up to the dissociation limit in the ground electronic state and are ignored for higher states. Rotational levels are ignored. The resulting *D/XB* increases with both electron density n_e (roughly logarithmically) and with electron temperature T_e (with a minimum at 5 eV and then increasing roughly linearly above 10 eV). n_e in the emission region is estimated from the measured $T_{rot}^{3p}(v' = 0)$ using the empirical scaling (dashed curve) of figure 6. From this n_e, a rough estimate for the electron temperature in the emission region can be determined from measured (n_e, T_e) profiles: edge probe data (cross-checked with core Thomson) is used for main chamber view chords (upper view chords and main chamber view chord in figure 1), while divertor Thomson is used for divertor view chords (lower view chords in figure 1. The (n_e, T_e) profile in the inner divertor leg is not known; for lack of better information, we assume here that the divertor Thomson (n_e, T_e) profile measured in the outer divertor leg also applies to the attached inner leg. This technique typically gives electron temperatures in the range $T_e \approx 10$– 70 eV in the D_2 emission region, depending on the viewing location and plasma conditions.

The local deuteron flux from D_2 influx can now be estimated as being $\Gamma_D(D_2) \approx f_{ion} I_{D_2}(D/XB)$, where I_{D_2} is the total Fulcher band brightness. Here, we define the deuteron flux as the flux of neutral deuterons coming from the wall, which enter the plasma and are converted to D^+. The scaling factor f_{ion} accounts for D neutrals lost back to the wall, e.g. if every D_2 entering the plasma edge ends up as two deuterium ions, then $f_{ion} = 2$. Under some conditions, one might expect electron-impact dissociation to be the dominant D_2 destruction process:

$$e + D_2 \rightarrow e + 2D, \tag{1}$$

in which case $f_{ion} \approx 1$, since half the fast Franck–Condon deuterons D are lost back to the wall, as *D*, being much hotter, has a longer mean-free-path than D_2. In TEXTOR experiments, it was concluded that the dominant D_2 destruction chain was actually electron-impact ionization into the molecular ion:

$$e + D_2 \rightarrow 2e + D_2^+, \tag{2}$$

followed by electron-impact dissociation of the molecular ion:

$$e + D_2^+ \rightarrow e + D^+ + D. \tag{3}$$

From the deuterons created in equation (3), it is expected that roughly half will go into the plasma and be ionized and 1/2 will go out and hit the wall; so, taking the TEXTOR results as a best available approximation for ionizing DIII-D edge conditions, we use $f_{ion} = 3/2$ here.

Squares in figure 7 show the fuelling flux Γ_D obtained from the spectrometer using Fulcher band brightnesses (estimated from the $v' = 0$ branch) as a function of emission volume poloidal angle θ (with $\theta = 0$ roughly corresponding to the divertor floor, $\theta = +/-1.5$ to the outer/inner midplane, see figure 1). The three cases shown differ primarily in plasma density. Data from 'reverse-B_T' discharges are used, where inner leg detachment is more difficult to achieve, so both divertor legs are believed to be mostly attached (ionizing) plasma in the data shown in figure 7. As expected, the Fulcher brightness is largest near the divertor strike points, although some signal is still observed in the main chamber. Also, it can be seen that the recycling flux increases strongly with increasing plasma density, with the maximum flux in the $(\bar{n}_e = 3.5 \times 10^{19}\ \mathrm{m}^{-3})$ line-averaged density case being $\approx 15\times$ larger than the maximum in

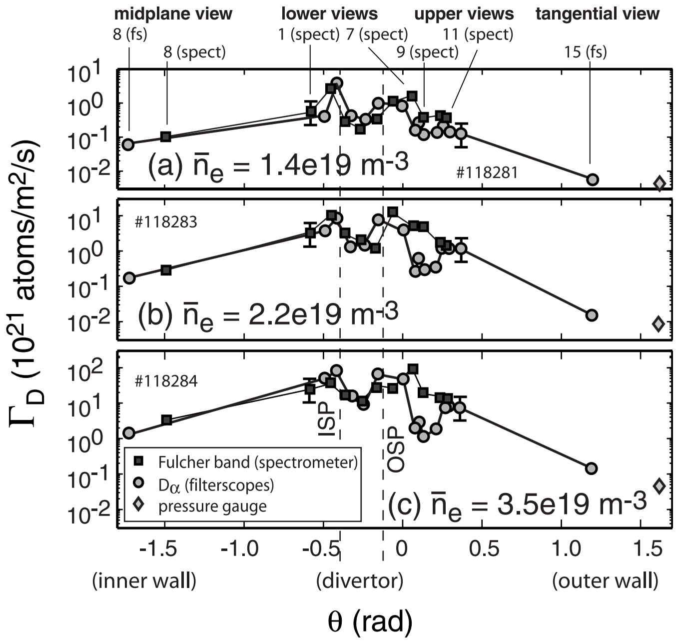

Figure 7. Deuteron fuelling flux versus poloidal angle θ for three different discharge densities. Select spectrometer channels (see figure 1) are labelled 8 (spect), 9 (spect), etc; analogous filterscope channels are labelled (fs).

the lowest density case ($\bar{n}_e = 1.4 \times 10^{19}\,\mathrm{m}^{-3}$), qualitatively consistent with the well-known n_e^{2-3} recycling scaling [26].

Circles in figure 7 show the fuelling flux Γ_D estimated from D_α emission measured with filterscopes. The filterscope view chord geometries used are similar to the spectrometer view chords shown in figure 1 but with 7 lower views, 6 upper views, a midplane view and a midplane tangential view. Γ_D from D_α emission is estimated in the usual way as $\Gamma_D(D_\alpha) \approx I_{D\alpha} \times (S/XB)$, where $I_{D\alpha}$ is the measured D_α brightness and S/XB is the D inverse photon efficiency (ionizations per D_α photon) [27]. For the purposes of evaluating S/XB, the D_α emission is assumed to be localized to the same (n_e, T_e) region as the D_2 emission in the same view chord. This is clearly very approximate, because of the difference in mean-free-path between the two species. However, S/XB for D_α is a relatively weak function of plasma parameters, (e.g. $S/XB \approx 7.0$ for $(n_e, T_e) = (10^{18}\,\mathrm{m}^{-3}, 10\,\mathrm{eV})$ and $S/XB \approx 16.2$ for $(n_e, T_e) = (10^{19}\,\mathrm{m}^{-3}, 40\,\mathrm{eV})$), while D/XB for D_2 is also a relatively weak function of plasma parameters (e.g. $D/XB \approx 400$ for $(n_e, T_e) = (10^{18}\,\mathrm{m}^{-3}, 10\,\mathrm{eV})$ and $D/XB \approx 2900$ for $(n_e, T_e) = (10^{19}\,\mathrm{m}^{-3}, 40\,\mathrm{eV})$]; so this co-localization approximation is expected to be reasonable for a qualitative comparison of D_2 and D fluxes, with the dominant error probably arising in the uncertainty of the electron temperature of the emission region. Characteristic error bars are shown in figure 7 assuming a factor of 2 uncertainty in the T_e of the emission region; it can seen that the resulting error in the fluxes is roughly a factor of 2 also.

The grey circles at $\theta = 1.2$ in figure 7 correspond to the fluxes Γ_D obtained just below the outer midplane from inversions of edge tangential D_α measurements. Additionally, a very preliminary estimate of the recycling flux at the outer midplane can be obtained from neutral pressure gauge measurements. The input aperture of this neutral pressure gauge is designed

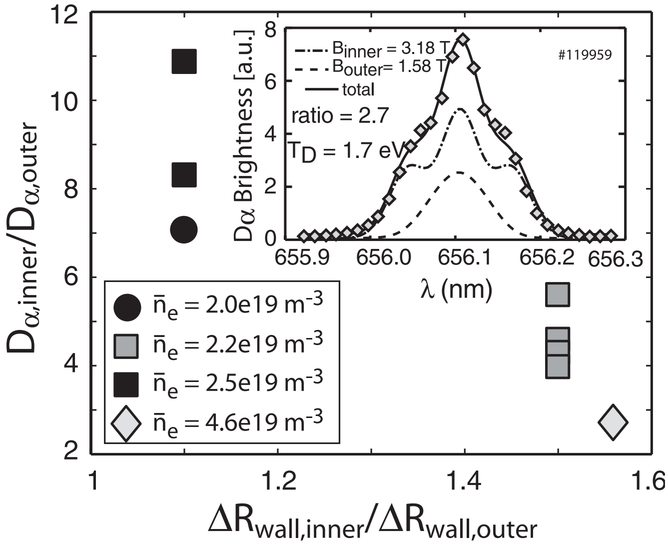

Figure 8. Ratio of inner midplane over outer wall (midplane chord) D_α emission as a function of inner wall gap over outer wall gap ratio. Insert shows sample D_α line profile and model components from inner and outer SOL.

to capture the outgoing flux of neutrals leaving the plasma outer midplane. This data is shown by the grey diamonds in figure 7. Here, we assume $\Gamma_D \approx \frac{1}{8}\frac{P}{T_{D2}}\sqrt{\frac{8T_{kin}}{\pi m}}$, where P is the pressure measured at the pressure gauge, $T_{kin} \approx 300$ K is a rough guess for the neutral temperature at the detector and the additional $2\times$ reduction relative to the typical neutral flux formula comes from neutral Monte-Carlo simulations indicating a $\approx 2\times$ correction factor due to neutral-wall collisions.

The data of figure 7 suggest a significant $\approx (5-20\times)$ asymmetry between inner and outer wall fuelling. This asymmetry in neutral flux is supported by line profile analysis of D_α emission measured by the midplane view chord. Available midplane L-mode data (with similar geometry to other shots studied here) and with the visible spectrometer set on D_α is shown in figure 8, where the ratio of inner to outer wall D_α emission is plotted as a function of the inner over outer wall gap ratio (with wall gap defined as distance between midplane separatrix and the wall). The D_α fits performed here assume (unpolarized measurement) Zeeman-split emission from both inner and outer midplane SOL regions using the known magnetic field strength at the inner and outer midplane SOL. The data suggest a $\approx$ (3–12$\times$) asymmetry between inner and outer midplane recycling, qualitatively consistent with the measurements of figure 7.

The insert of figure 8 shows a sample D_α line profile fit assuming a single Gaussian line shape with temperature $T_D = 1.7$ eV, convolved with the instrumental response. The average deuteron temperature obtained from these single-temperature fits is typically $T_D \approx$ 1–2 eV. This low deuteron temperature suggests that the midplane D_α emission is dominated by atoms created locally by D_2 breakup [28]. The total D_α line shape is also expected to contain a hot ($T_D \approx$ 10–50 eV) component from charge-exchange; however, confidently resolving this smaller hot component is difficult for this data set.

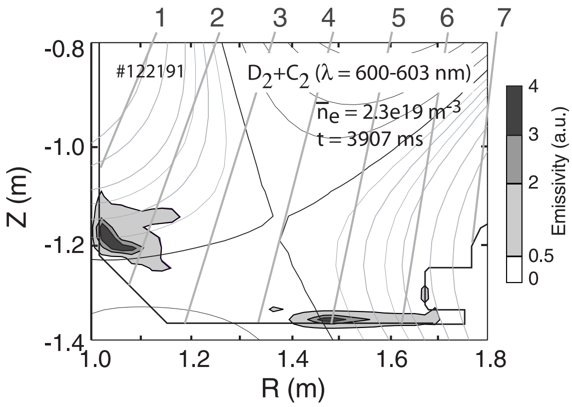

Figure 9. Inversion of D_2 plus C_2 emission from a plasma with detached inner divertor leg and attached outer leg.

5. Spatial distribution of D_2

The spectrometer data of figure 7 indicate that D_2 emission is strongest near the lower divertor strike points. This is in agreement with divertor camera image inversions made using a D_2 filter. Figure 9 shows the qualitative distribution of D_2 emissivity for a toroidal slice across the lower divertor with magnetic flux surfaces overlaid. A forward-B_T discharge is shown, where the inner divertor leg detaches quite easily—even at the low line-averaged density shown here, the inner divertor leg is believed to be detached or nearly detached while the outer leg remains attached. As expected, the D_2 emission can be seen to extend farther into the inner divertor leg than the outer divertor leg, consistent with a colder plasma with longer ionization mean free path.

The inversion in figure 9 is expected to give only a very qualitative impression of the D_2 localization because up to about half of the measured signal could come from C_2 in some emission regions. The narrowband interference filter used had FWHM ≈ 3.3 nm centered at 601.8 nm; the transmission curve of this filter is shown by the grey line in figure 3. Over the band pass of the filter, lines of the $v' = 0$ Fulcher band are the most prominent spectral features. Smaller lines, however, could contribute significantly to the measured signal over the band pass of the filter ($\lambda \approx 600$–603 nm); these hard-to-identify smaller lines are believed to be other D_2 lines (e.g. P and R Fulcher branches and vibrationally non-diagonal transitions) and C_2 lines from the $(v' = 3, v'' = 5)(\lambda \approx 600\,\text{nm})$ branch of the Swan band $(d^3\,\Pi - a^3\,\Pi)$ [29]; two of these lines are tentatively identified in figure 3. An approximate upper bound on the relative C_2 contribution to the image of figure 9 was obtained by measuring a spectrum at the $\approx 10\times$ stronger band head ($\Delta v = 0, \lambda \approx 516$ nm) and comparing this with the measured spectrum at $\lambda \approx 600$ nm (using shots #122197 and #119922, which were similar to the shot of figure 9). This comparison gives $I(C_2)/I(D_2) \approx 0.6$ away from the divertor (Chord 1 in figure 9) and $I(C_2)/I(D_2) \approx 1.2$ at the outer strike point (Chord 5 in figure 9). $I(C_2)/I(D_2)$ is the estimated Swan band/Fulcher band Q-branch brightness ratio integrated over the filter band pass. This is a worst-case upper bound on the relative effect of C_2 emission, since the contribution of the many smaller D_2 lines has been neglected.

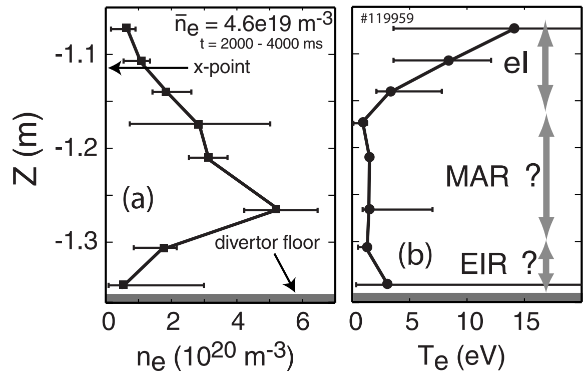

Figure 10. Divertor Thomson data of detached outer leg showing (*a*) n_e and (*b*) T_e. Large error in T_e at lowest vertical location suggests $T_e < 1$ eV.

6. Effect of D_2 on volume recombination

In divertor plasmas, a wide range of collision processes involving hydrogen neutrals and ions can occur (see for example [30]). For simplicity, we categorize these coarsely as collisional excitation and ionization processes (eI): processes leading to recombination of the molecular ions H_2^+, H_3^+ and the negative ion H^- (MAR) and radiative or three-body recombination of H^+ (EIR). For typical detached divertor densities $n_e \approx 10^{19}$–10^{20} m^{-3}, eI usually dominates for $T_e > 3$ eV, MAR for $0.5 < T_e < 3$ eV and EIR for $T_e < 0.5$ eV [7]. Thus, all three processes can occur at the same time in different parts of a divertor leg. A potential example of this is shown in figure 10, where divertor Thomson data is shown for a similar magnetic geometry to that of figure 9 but during a high density ($\bar{n}_e = 4.6 \times 10^{19}$ m^{-3}) L-mode forward-B_T discharge in which both divertor legs are strongly detached. It can be seen that the divertor temperature, figure 10(*b*), transitions from $T_e > 3$ eV up near the x-point, through a 1 eV region in the middle of the divertor leg, to a region with $T_e < 1$ eV (not resolved by the Thomson system) just above the strike point. Expected dominant processes (eI, MAR and EIR) in each region are labelled in figure 10(*b*). eI, MAR and EIR processes all emit D_α light, and inversions of divertor D_α camera images of detached divertors have shown that D_α emission is widely distributed throughout the divertor [31], suggesting that all three of these processes might be occurring.

To estimate the magnitude of the recombination sink associated with EIR in the detached divertor of figure 10, measured D_γ brightnesses are used, together with an *R/XB* (recombinations/photon) conversion factor from collisional-radiative modelling [32]. This *R/XB* factor varies with n_e and T_e in the EIR emission region. n_e is estimated from Thomson data taken immediately above the divertor floor ($Z = -1.35$ m) during strike point sweeps. $T_e \approx 0.5$ eV is used as a rough guess for the electron temperature, since the huge error in the Thomson data fit indicates $T_e < 1$ eV, and preliminary analysis of high-*n* Balmer lines measured at the outer strike point with the survey and near-UV spectrometers gives values in the range $T_e \approx 0.2$–0.6 eV (assuming local thermal equilibrium between free and high-*n* bound electrons). This large uncertainty in T_e does not greatly affect the resulting recombination rate, i.e.$T_e \approx 0.2$–0.6 eV and $n_e \approx 10^{20}$ m^{-3} give $R/XB(D_\gamma) \approx 65$–$51$.

To estimate the magnitude of MAR in the detached divertor region, D_2 influxes calculated from Fulcher brightnesses are used. As discussed above, MAR encompasses a variety of

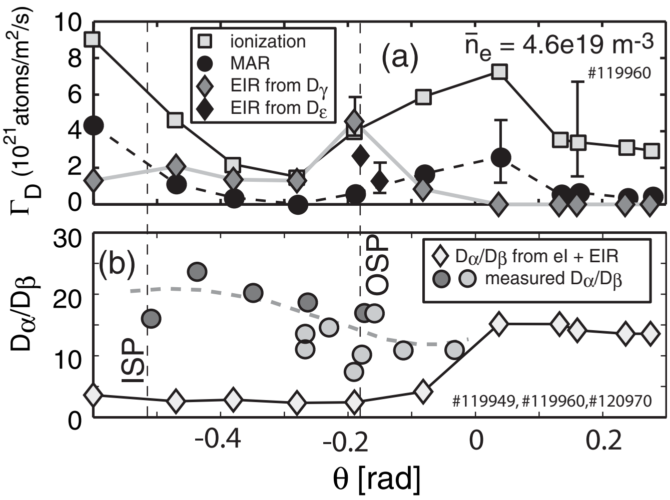

Figure 11. (*a*) Detached divertor volume sources and sinks estimated from spectroscopy and (*b*) measured and predicted divertor D_α/D_β ratios.

processes; however, the conversion of D^+ into D_2^+ by charge-exchange,

$$D^+ + D_2 \rightarrow D + D_2^+, \tag{4}$$

followed by dissociative recombination of D_2^+,

$$e + D_2^+ \rightarrow D + D^*, \tag{5}$$

is typically thought to be the dominant MAR sequence [7]. The fraction of inflowing D^+ ions converted to D_2^+ can then be estimated to be roughly $f_{CX} \approx 1 - \exp(-\nu_{CX}L/\bar{v}_i)$, where $\nu_{CX} = n_{D2}\langle\sigma_{CX}v_i\rangle$ is the (T_{vib}-resolved) charge exchange rate, $v_i \approx 10^4\,\mathrm{m\,s^{-1}}$ is the ion velocity and $L \approx 2\,\mathrm{m}$ is an approximate ion path length through the MAR region (assuming a simple trajectory along field lines and ignoring cross-field transport, drifts, etc). Similarly, the fraction of resulting D_2^+ ions which recombine before flowing into the divertor plate is roughly $f_{DR} \approx 1 - \exp(-\nu_{DR}L/\bar{v}_i)$, where ν_{DR} is the dissociative recombination rate of D_2^+ (process (DR)). In evaluating ν_{DR}, the fraction of D^* in equation (5) which is re-ionized is not counted; this fraction is negligible at $T_e = 1\,\mathrm{eV}$ but becomes important for $T_e > 3\,\mathrm{eV}$. Typically, (DR) is very rapid and $f_{DR} \approx 1$. Because of this, recombination into excited states of D_2 (i.e. recombination light into Fulcher emission) is expected to be negligible. The deuteron flux going into MAR is then estimated as being $\Gamma_{MAR} = f_{CX}f_{DR}\Gamma_D$. The local neutral molecule density (of order $n_{D2} \approx 10^{18}\mathrm{m^{-3}}$) is estimated from the flux using $\Gamma_{D2} = n_{D2}v_{D2}$, with $\Gamma_{D2} \approx 10^{21}\,\mathrm{m^2\,s^{-1}}$ and $v_{D2} \approx 10^3\,m\,s^{-1}$. As a rough guess for the molecular deuterium velocity, the D_2 kinetic temperature is assumed to equal the ground state rotational temperature: $T_{kin} \approx T_{rot}^{1s}(v=0) \approx 2T_{rot}^{3p}(v'=0)$. Typically, this is expected to overestimate T_{kin} somewhat [21], although the measured linewidths of the D_2 lines in these experiments suggest that $T_{kin} = T_{rot}^{1s}(v=0)$ within a factor of 2. Zeeman splitting of Fulcher band lines was neglected here; this is thought to be small but fairly complicated to account for, as it can vary with the rovibrational state of D_2 [33].

Figure 11 (*a*) shows estimated ionization and recombination sinks across the detached divertor for the conditions shown in figure 10. Squares show the ionization flux, calculated from the Fulcher brightness as discussed in sections 3 and 4, while circles show MAR recombination flux and diamonds show EIR recombination flux. The two black diamonds are EIR rates calculated from D_ε measured by the near-UV and survey spectrometers. These serve as good cross-checks of the D_γ measurements, since D_ε emission is expected to be more completely populated by EIR. It can be seen that MAR appears to result in a particle sink which is roughly 2× smaller than the ionization source and is roughly comparable to EIR in magnitude, when averaged over the divertor. As discussed earlier, both MAR and ionization fluxes are calculated from the measured D_2 brightness; the changing ratio ≈ 2–10× between the two results dominantly from changes in the ion conversion fraction f_{CX}, which in turn varies here primarily with measured $T_{kin} \approx 2T_{rot}^{3p}(v' = 0)$. As in figure 7, characteristic error bars are estimated here based on the assumption that the dominant source of error in the deuteron flux is a factor of 2 uncertainty in the T_e of the emission region. This gives an error of about 2× in the estimates of ionization and MAR sources/sinks and a somewhat smaller error (about 30%) in the estimated EIR sink.

Figure 11(*b*) shows the Balmer D_α/D_β ratio measured in the divertor using filterscopes (with views similar to the lower view chords of figure 1). Dark-filled circles are data where the strike points were held fixed (shot #119960), while the light-filled circles are data mapped from similar discharges with strike point sweeps (shots #119949 and #120970). The diamonds in figure 11 (*b*) show the D_α/D_β ratio expected assuming only eI and EIR processes; the eI D_α and D_β brightnesses are obtained from the measured D_2 brightness (ignoring MAR and using best estimates of the local plasma parameters in the ionizing emission region to estimate Balmer emission resulting from D_2 influx into ionizing plasma), while the EIR D_α and D_β brightnesses are estimated from the measured D_γ brightness. Overall, the data demonstrate that the measured line-integrated D_α/D_β ratio is not consistent with an EIR-dominated recombining divertor. It is possible, however, that including MAR (not included in the D_α/D_β calculation) could help resolve this discrepancy, since process (DR) is expected to have $D_\alpha/D_\beta \approx 10$–15, which is close to the measured values of figure 11 (*b*). Overall, the D_α/D_β ratio is a complicated function of plasma parameters, so separating out eI, MAR and EIR processes accurately will require more accurate data and modelling.

7. Discussion

The ionizing plasma results of section 4 indicate that a significant fraction of the fuelling flux into the plasma SOL comes from D_2, as opposed to only from D. This is based on the observation that Γ_D is roughly the same when obtained from D_α or from Fulcher emission, i.e. $\Gamma_D(D_\alpha) \approx \Gamma_D(D_2)$ (figure 7); if the fuelling flux came dominantly from D, one would expect $\Gamma_D(D_\alpha) >> \Gamma_D(D_2)$ [34]. Because the D/XB factor used to convert D_2 emission into D_2 flux increases slowly (linearly) with T_e in ionizing plasma, the uncertainty in the location of the D_2 emission region in these measurements is not expected to invalidate this conclusion; for example, if the D_2 emission occurs from a region with $T_e = 20$ eV rather than $T_e = 10$ eV, the resulting estimated D_2 flux would increase only by a factor of 2 or so. In L-mode, the walls in DIII-D are observed to remain quite cold ($T_{wall} < 500$ K) in both the divertor and main chamber regions. These results are therefore consistent with previous measurements made in front of a graphite test limiter in TEXTOR which indicate that, for cold ($T_{wall} < 1000$ K) wall conditions, recycled deuterons released from graphite under D^+ flux are dominantly (> 90%) in the form of D_2 neutrals (as opposed to, for example, thermal release of D or reflection of D^+) [24]. This is also expected to apply to cold graphite under atomic D flux, i.e. we cannot distinguish here between D_2 released from the wall as a result of local D^+ flux and D_2 released from the wall after bombardment by D. As a result, the data presented here are inconclusive on the important question of main chamber versus divertor recycling because the D_2 observed in the midplane could come from D charge-exchange diffusing up along the vessel wall from the divertor. However, the observation that main chamber fuelling comes dominantly from the inboard (high field) side seems to contradict the presence of significant main-chamber recycling (D^+flux), since main chamber SOL turbulence (and radial flux) is typically thought to have a ballooning nature and thus be larger on the low field side of the vessel [35]. However, these conclusions could very well be geometry-specific, i.e. depend on the height of the x-point, location of inner divertor strike point, inner/outer wall gaps, etc. Additionally, all the main chamber data of section 4 are taken at toroidal locations far from the outer midplane bumper limiters, so the inner/outer asymmetry of figure 8 does not necessarily apply at all toroidal angles.

The results of section 6 indicate that MAR could be important in detached DIII-D divertors. This is based on estimates using observed D_2 and Balmer brightnesses, which suggest that MAR and EIR are comparable in magnitude (figure 11(*a*)). Additional supporting evidence comes from the measured D_α/D_β ratio in the divertor, which is more consistent with MAR than with EIR (figure 11(*b*)). However, many possible uncertainties remain in this data (in addition to the estimates of the measurement error shown in figure 11(*a*)). At the very large internal D_2 energies observed, with $T_{vib} \approx 30\,000$ K approaching the D_2 dissociation energy, it is unlikely that the distribution of vibrational levels is actually well described by a single temperature, as was assumed here; so v-resolved modelling is probably necessary for accurate determination of rate coefficients [8]. Additionally, there are still significant uncertainties in calculated rate coefficients: for example, some estimates of MAR processes have indicated that D_2^+ destruction exceeds D_2^+ formation (CX) even at low electron temperatures $T_e \approx 1$ eV, in which case MAR might not be as large as estimated here [8]. On the other hand, D^- formation has not been included here; this might become significant at $T_{vib} \approx 30\,000$ K and could increase the MAR rate. Also, low Balmer ratios $D_\alpha/D_\beta \approx 5$ consistent with EIR-dominated divertors have been observed previously in some view chords in DIII-D; however these measurements were obtained in H-mode discharges and using tangential views of the lower divertor [36]. A different previous study using vertical views and measuring D_β/D_γ ratios was inconclusive, giving ratios roughly halfway between EIR and eI [31]. Additionally, Ly_α opacity has been ignored here. Detached divertor plasmas are frequently opaque to Ly_α [37,38], and this opacity can affect hydrogen recombination and ionization as well as corresponding emission rates. However, estimates made in very high density ($n_e \approx 10^{21}$ m^{-3}) detached divertor plasmas in Alcator C-Mod indicated that molecular effects could maintain their importance even for 99% opaque divertor plasmas [39]. Overall, the detached divertor results presented here suggest that MAR could be an important sink of ions in DIII-D detached plasmas, but confirmation of this will require better spatially-resolved data and more complete atomic physics modelling.

In conclusion, analysis of D_2 spectral data has shown that D_2 is found in significant quantities throughout the edge region of DIII-D discharges, consistent with molecular deuterium released from cold graphite walls. In detached divertor operation, D_2 in the divertor is observed to be excited into high rotational and vibrational levels, indicating that molecular ion formation could be significant. Although these results were performed in L-mode plasmas, the effects discussed here could also be important during H-mode operation. Preliminary (slow) measurements indicate that D_2 is also found throughout the edge region of DIII-D in H-mode discharges, indicating that H-mode recycling, at least in a time-averaged sense, releases significant quantities of molecular deuterium, which could, in principle, help spread ELM heat loads and prevent ELM burn-through of detached divertor legs. Assessing the effects of D_2 on divertor and edge dynamics during ELMs will be pursued in future research.

Acknowledgments

The advice and comments of S L Allen, J C DeBoo, A G Kellman, S Lisgo and G Sergienko, probe data analysis of R A Moyer and J G Watkins and technical support of the DIII-D team are gratefully acknowledged. This work was supported by the US Department of Energy under DE-FG02-04ER54758, DE-FC02-04ER54698 and W-7405-ENG-48.

References

[1] Unterberg B *et al* 2005 *J. Nucl. Mater.* **337** 515
[2] Sugihara M *et al* 1999 *J. Nucl. Mater.* **266** 691
[3] Pigarov A Yu *et al* 2003 *J. Nucl. Mater.* **313** 1076
[4] Groth M *et al* 2005 *J. Nucl. Mater.* **337** 425
[5] Lipschultz B *et al* 2005 *Plasma Phys. Control. Fusion* **47** 1559
[6] Groebner R J *et al* 2004 *Nucl. Fusion* **44** 204
[7] Pigarov A Yu 2002 *Phys. Scr.* **T96** 16
[8] Fantz U, Reiter D, Heger B and Coster D 2001 *J. Nucl. Mater.* **290** 367
[9] Kubo H *et al* 2005 *J. Nucl. Mater.* **337** 161
[10] Luxon J L 2002 *Nucl. Fusion* **42** 614
[11] Brooks N H, Howard A, Klepper K and West P 1992 *Rev. Sci. Instrum.* **63** 5167
[12] Carlstrom T N *et al* 1997 *Rev. Sci. Instrum.* **68** 1195
[13] Watkins J G *et al* 1997 *Rev. Sci. Instrum.* **68** 373
[14] Fenstermacher M E *et al* 1997 *Rev. Sci. Instrum.* **70** 974
[15] Groth M *et al* 2003 *Rev. Sci. Instrum.* **74** 2064
[16] Brezinsek S *et al* 2003 *J. Nucl. Mater.* **313** 967
[17] Fantz U and Heger B 1998 *Plasma Phys. Control. Fusion* **40** 2023
[18] Herzberg G 1950 *Spectra of Diatomic Molecules* (New York: D Van Nostrand Co)
[19] Qing Z *et al* 1996 *J. Appl. Phys.* **80** 1312
[20] Xiao B, Kado S, Kajita S and Yamasaki D 2004 *Plasma Phys. Control. Fusion* **46** 653
[21] Brezinsek S 2002 Study of atomic and molecular hydrogen in front of a graphite surface in a high-temperature edge plasma *PhD Thesis* Forschungszentrum Juelich
[22] Hollmann E M, Pigarov A Yu and Taylor K 2005 *J. Nucl. Mater.* **337** 451
[23] Lavrov B P and Otorbaev D K 1978 *Opt. Spektrosk.* **45** 1074
[24] Brezinsek S *et al* 2005 *Plasma Phys. Control. Fusion* at press
[25] Greenland P T *Contrib. Plasma Phys.* **42** 608
[26] Pitcher C S and Stangeby P C 1997 *Plasma Phys. Control. Fusion* **39** 779
[27] Summers H P 1994 Atomic data and analysis structure—user's manual *JET Joint Undertaking Report* JET-IR94
[28] Janev R K *et al* 1984 *J. Nucl. Mater.* **121** 10
[29] Brezinsek S *et al* 2005 *J. Nucl. Mater.* **337–339** 1058
[30] Janev R K, Reiter D and Samm U 2003 Collision processes in low-temperature hydrogen plasmas *Forschungszentrum Jülich Report* Jül-4105 (Jülich)
[31] Isler R C *et al* 1997 *Phys. Plasmas* **4** 2989
[32] Reiter D 1992 *J. Nucl. Mater.* **196–198** 80
[33] Sergienko G, Pospieszczyk A and Rusbuelt D 1996 *Proc. of the 23rd EPS Conf. On Controlled Fusion and Plasma Physics (Kiev, Ukraine)*
[34] Pospieszczyk A *et al* 2005 *J. Nucl. Mater.* **337** 500
[35] Terry J L *et al* 2003 *Phys. Plasmas* **10** 1739
[36] Isler R C *et al* 1999 *Phys. Plasmas* **6** 541
[37] Terry J L *et al* 1999 *J. Nucl. Mater.* **266-269** 30
[38] Pigarov A Yu, Terry J L and Lipschultz B 1998 *Plasma Phys. Control. Fusion* **40** 2055
[39] Terry J L *et al* 1998 *Phys. Plasmas* **5** 1759